A&A 624, A42 (2019)
https://doi.org/10.1051/0004-6361/201834600

Astronomy & Astrophysics

Accretion disk versus jet orientation in H_2O megamaser galaxies

F. Kamali[1,⋆], C. Henkel[1,2], S. Koyama[3,1], C. Y. Kuo[4], J. J. Condon[5], A. Brunthaler[1], M. J. Reid[6], J. E. Greene[7], K. M. Menten[1], C. M. V. Impellizzeri[5,8], J. A. Braatz[5], E. Litzinger[9,10], and M. Kadler[9]

[1] Max-Planck-Institut für Radioastronomie, Auf dem Hügel 69, 53121 Bonn, Germany
e-mail: fkamali@mpifr-bonn.mpg.de, fateme.kamali28@gmail.com
[2] Astron. Dept., King Abdulaziz University, PO Box 80203, Jeddah 21589, Saudi Arabia
[3] Academia Sinica Institute of Astronomy and Astrophysics, PO Box 23-141, Taipei 10617, Taiwan
[4] Physics Department, National Sun Yat-Sen University, No. 70, Lien-Hai Rd, Kaosiung City 80424, Taiwan
[5] National Radio Astronomy Observatory, 520 Edgemont Road, Charlottesville, VA 22903, USA
[6] Harvard-Smithsonian Center for Astrophysics, 60 Garden Street, Cambridge, MA 02138, USA
[7] Department of Astrophysical Sciences, Princeton University, Princeton, NJ 08544, USA
[8] Joint ALMA Office, Alonso de Córdova 3107, Vitacura, Santiago, Chile
[9] Institut für Theoretische Physik und Astrophysik, Universität Würzburg, Campus Hubland Nord, Emil-Fischer-Str. 31, 97074 Würzburg, Germany
[10] Dr. Remeis-Observatory, Erlangen Centre for Astroparticle, Physics, University of Erlangen-Nuremberg, Sternwartstr. 7, 96049 Bamberg, Germany

Received 7 November 2018 / Accepted 11 February 2019

ABSTRACT

Context. An essential part of the paradigm describing active galactic nuclei is the alignment between the radio jet and the associated rotation axis of the sub-pc accretion disks. Because of the small linear and angular scales involved, this alignment has not yet been checked in a sufficient number of low luminosity active galactic nuclei (LLAGNs).
Aims. The project examines the validity of this paradigm by measuring the radio continuum on the same physical scale as the accretion disks to investigate any possible connection between these disks and the radio continuum.
Methods. We observed a sample of 18 LLAGNs in the 4.8 GHz (6 cm) radio continuum using the Very Long Baseline Array (VLBA) with 3.3–6.5 ms resolution. The sources were selected to show both an edge-on accretion disk revealed by 22 GHz H_2O megamaser emission and signatures of a radio jet. Furthermore, the sources were previously detected in 33 GHz radio continuum observations made with the Very Large Array.
Results. Five out of 18 galaxies observed were detected at 8σ or higher levels (Mrk 0001, Mrk 1210, Mrk 1419, NGC 2273, and UGC 3193). While these five sources are known to have maser disks, four of them exhibit a maser disk with known orientation. For all four of these sources, the radio continuum is misaligned relative to the rotation axis of the maser disk, but with a 99.1% confidence level, the orientations are not random and are confined to a cone within 32° of the maser disk's normal. Among the four sources the misalignment of the radio continuum with respect to the normal vector to the maser disk is smaller when the inner radius of the maser disk is larger. Furthermore, a correlation is observed between the 5 GHz VLBA radio continuum and the [OIII] luminosity and also with the H_2O maser disk's inner radius.

Key words. galaxies: active – galaxies: jets – galaxies: ISM – galaxies: nuclei – galaxies: Seyfert – radio continuum: galaxies

1. Introduction

Accretion of material onto the central engine of an active galactic nucleus (AGN) is often accompanied by ejection of material, either in the form of outflows or collimated jets. Conservation of angular momentum implies that the distribution of any material ejected from the accretion disk surrounding the supermassive black hole (SMBH) should be perpendicular to the disk unless an external torque is present. On the other hand, studies have shown that the jet direction and the rotation axis of the large-scale galactic disk are not necessarily aligned (e.g., Pringle et al. 1999; Nagar & Wilson 1999). Further studies have been carried out to investigate the alignment of the jet axis with the vector perpendicular to the smaller 20–150 pc scale disks such as dust disks in active galaxies, and have reported that the jets are not always perpendicular to these disks (Schmitt et al. 2002). This misalignment indicates that gas on different scales has different angular momentum orientations. Whether this is a result of past mergers or warping of the accretion disk, or a general physical condition required for accretion, is still a matter of debate (see Greene et al. 2010, and references therein). With the discovery of H_2O maser emission from the water vapor $J_{K_-K_+} = 6_{16} - 5_{23}$ rotational transition in the sub-pc disk surrounding the SMBH in NGC 4258 (e.g., Nakai et al. 1993; Greenhill et al. 1995; Miyoshi et al. 1995; Herrnstein et al. 1999), an opportunity arose to observe the accretion disk of AGNs with the extremely high angular resolution only offered by Very Long Baseline Interferometry (VLBI) observations. The other unique feature of galaxies with H_2O masers in their nuclear accretion disk is that these accretion disks are viewed within a few degrees edge-on, otherwise linear scales for coherent amplification would be too short, and thus we expect the putative jets

⋆ Member of the International Max Planck Research School (IMPRS) for Astronomy and Astrophysics at the Universities of Bonn and Cologne.

to be on the plane of the sky and free of viewing angle biases. Therefore, the nuclear region of galaxies hosting maser disks are good laboratories for studying the alignment between the jet and the normal to the pc-size disks. Greene et al. (2013) and Pjanka et al. (2017) investigated this alignment by observing the radio continuum jets on >50 pc scales. They also observed the structures such as galaxy-scale disks, bars, and spiral arms on <5 kpc scales and compared the alignment of these structures with the smaller scale sub-pc maser disks. They reported that the orientation of the 100 pc scale disks and galaxy scale disks are distributed randomly with respect to the orientation of the maser disks. However, the radio continuum jets (observed on tens of pc to kpc scale) are found to align within <15° of the maser disk's rotation axis (Greene et al. 2013). With the purpose of investigating the jet-disk alignment on smaller scales (~2 pc) and also of providing a larger sample compared to that already existing in the literature, in this work we attempt to study the alignment of the jet and the rotation axis of the accretion disk in low luminosity active galactic nuclei (LLAGN) with H_2O megamaser disks seen approximately edge-on. Recently we have observed a sample of 24 such galaxies with a resolution of 0.″2–0.″5 using the Karl G. Jansky Very Large Array (VLA) at 33 GHz in a pilot project (Kamali et al. 2017). Radio synchrotron emission was detected on kpc scales in 21 of these galaxies. In the follow-up observations presented here, we look for radio emission on scales of <50 pc (~5 mas or ~2 pc resolution at a fiducial distance of 90 Mpc) using the Very Long Baseline Array (VLBA). We chose *C* band because the synchrotron emission is supposedly brighter at this lower frequency compared to the previous VLA *Ka*-band observations. Our goal is to measure the radio continuum and investigate the relation between the jet axis and the maser disk orientation. This paper is organized in the following way: In Sect. 2 we present our sample. In Sect. 3 we present the observations and data reduction process. The description of the observational results is presented in Sect. 4, followed by analysis and subsequent discussions in Sect. 5. A summary is given in Sect. 6.

2. Sample

We selected a sample of 18 LLAGNs with declinations greater than −5°, including 14 sources from our 33 GHz survey (Kamali et al. 2017) plus four more from the Megamaser Cosmology Project (MCP, e.g., Reid et al. 2009, 2013; Braatz et al. 2010; Greene et al. 2010; Kuo et al. 2011, 2013; Pesce et al. 2015; Gao et al. 2017). These sources have signatures of megamasers disks, i.e., they show three groups of H_2O megamaser emissions in their spectrum; one set of maser features has velocities grouped around the recession velocity of the galaxy, and those of the two other sets of maser features are offset from this recession velocity, representing the approaching and receding sides of the disk. In our selected sample, 12 sources are considered "clean disks", where the maser emission from the disk dominates over any other maser emission from the jets or outflows (Pesce et al. 2015). These sources are shown in boldface in all tables. The maser emission in six other sources of our sample may not arise from the disk, but rather from the nuclear outflows or star forming regions in these galaxies. Detections for three out of these six non-clean disks are reported in this work. The maser distributions in two of these three galaxies (Mrk 0001 and Mrk 1210) have been mapped using the VLBI and the consequent fitting of disk models does not rule out a disk maser scenario (see Sect. 4.1 for further details on the maser disk observations for the individual sources). Therefore, since it is unclear whether either of the scenarios applies (the maser emission may actually arise from the disks), we consider all the sources as maser disks and our analysis is based on this assumption. The MCP is an ongoing project and the maser disk properties such as disk sizes and orientations have not yet been measured for all the candidates. For instance, the distances measured by the MCP (which are among the most accurate ones), are only available for four sources in our sample. These distances are in agreement within uncertainties with the distances listed in the NASA/IPAC Extragalactic Database (NED)[1]. For consistency we adopted the NED distances since they are available for all sources in our sample. The NED distances were obtained using $H_0 = 70.0\,\mathrm{km\,s^{-1}\,Mpc^{-1}}$, $\Omega_{\mathrm{matter}} = 0.27$, and $\Omega_{\mathrm{vacuum}} = 0.73$ as the cosmological parameters. H_2O maser luminosities from the literature were also rescaled to $H_0 = 70.0\,\mathrm{km\,s^{-1}\,Mpc^{-1}}$ to be consistent with other luminosities in this work.

3. Observations and data reduction

Our sample was observed between October and November 2015 using the VLBA in *C* band. The synthesized beamwidth was in the range from 3.3 to 6.5 mas. We used a total bandwidth of 128 MHz (2 × 64 MHz IFs, 4.644–4.708 GHz and 4.836–4.900 GHz) and right-hand circular polarization. The sources were grouped into six sets of three for observation, with a total time of 7 h per group and an integration time of ~1.5 h per target after (i.e., excluding) calibration. Our observations included two scans of fringe finders, one placed at the beginning and one at the end of the observations. The sources and their associated calibrators were observed alternating in scans of ~1 min. Table 1 indicates fringe finders and calibrators, and the J2000 coordinates obtained from previous VLA observations. Of the 18 observed sources, 5 were detected at a signal-to-noise ratio (S/N) of 8 or higher. In the case of four of these detected sources, Mrk 0001, Mrk 1210, Mrk 1419, and UGC 3193, the initial images did not have a sufficiently high quality. Therefore, to check our detections and obtain higher S/N values, we re-observed them with the VLBA in *C* band, between October and November 2017. This time they were grouped in two sets of two sources, with a total time of 8 h per group (2.5 h on-source per target, after calibration), bandwidth of 256 MHz (8 × 32 MHz IFs, from 4.836 to 5.092 GHz) and dual polarization.

The data were calibrated using the Astronomical Image Processing System (AIPS) software package developed by the National Radio Astronomy Observatory (NRAO). At first, the ionospheric dispersive delays and the Earth orientation parameters were corrected using AIPS tasks VLBATECR and VLBAEOPS, respectively. Then, using the task CLCOR, the parallactic angle correction was applied. The visibilities were normalized by the auto-correlations with the task ACCOR. The instrumental phases and delays were removed using the fringe finders listed in Table 1 and task VLBAMPCL. Amplitude corrections were applied using system temperature and the antenna gain information by the APCAL task in AIPS. We solved phases, delays, and rates by performing fringe fitting on the calibrators listed in Table 1 assuming a point source model, and applied the solutions to the targets.

For imaging, we used the task IMAGR in AIPS. Different weighting functions (including tapering of the *uv*-distances) were tried to find the optimum solution for a better S/N.

[1] https://ned.ipac.caltech.edu/

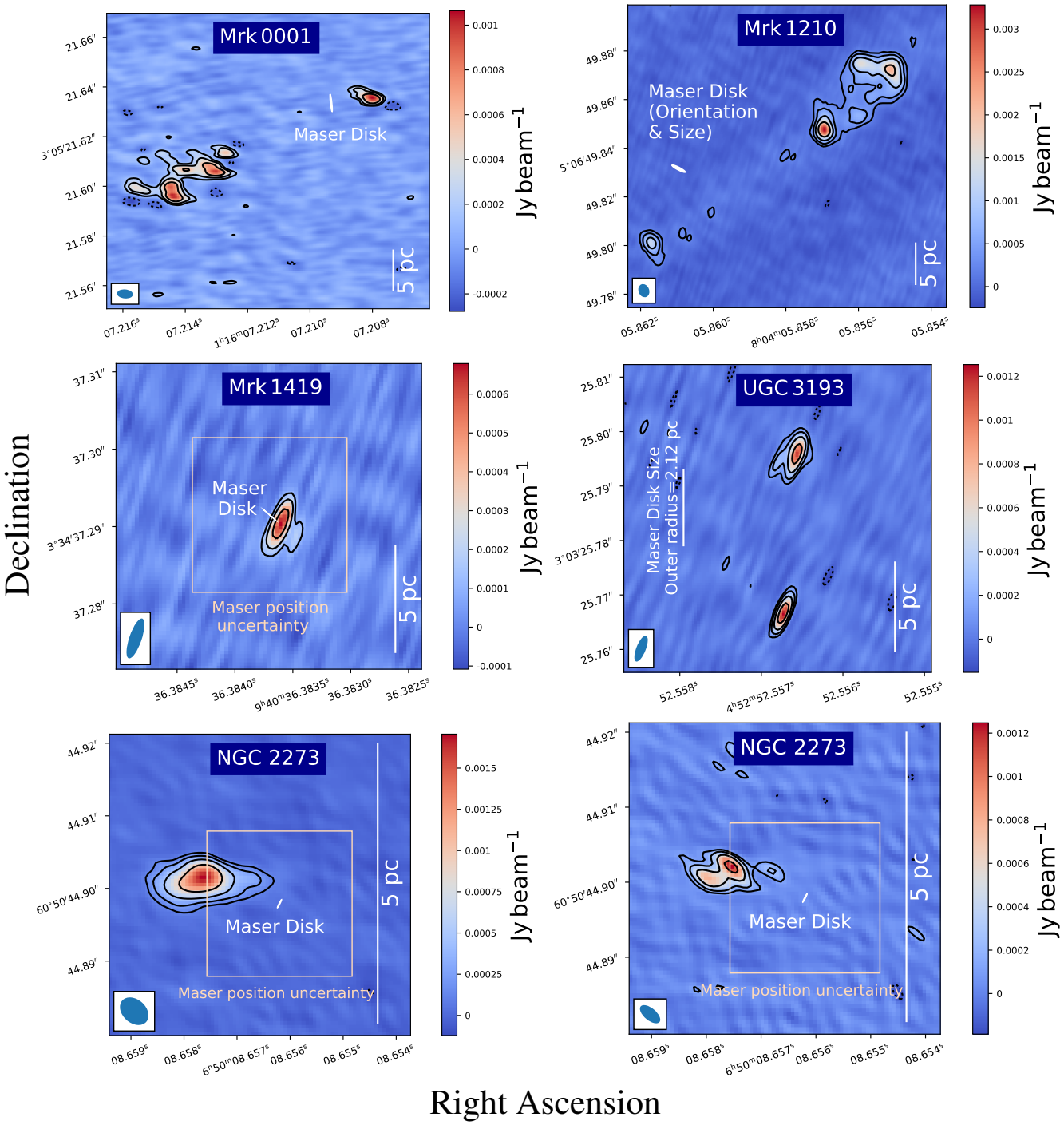

Fig. 1. 5 GHz contour maps. The contour levels are ±3, 6, 12, and 24 times the rms given in Table 3. The synthesized beam is shown in the lower left corner of each plot. For UGC 3193 the maser disk size; for Mrk 1210 the maser disk size and orientation; and for Mrk 0001, Mrk 1419, and NGC 2273 the maser disk size, orientation, position, and position uncertainties (light orange squares) are shown. For Mrk 0001 the maser position uncertainty is small. For Mrk 1210 and UGC 3193 the positions of the maser disks are not yet known. For NGC 2273, two contour maps using different Briggs weighting functions are shown: robust parameter 5, which is a pure natural weighting (*left panel*) and 0, which is between natural and uniform (*right panel*).

4. Results

Out of 18 sources observed, 5 were detected: Mrk 0001, Mrk 1210, Mrk 1419, NGC 2273, and UGC 3193. Figure 1 shows the 5 GHz radio continuum maps. For all images, phase self-calibration was employed to improve the image quality, using a solution interval of 1 min. For Mrk 0001 the S/N was improved from 8 to 32, for Mrk 1210 from 36 to 62, for Mrk 1419 from 12 to 18, for NGC 2273 from 56 to 61, and for UGC 3193 from 8 to 36. For detected sources we fitted two-dimensional Gaussians on the individual components using the task JMFIT in AIPS in order to obtain source properties such as peak and integrated flux, position, and its uncertainty (when the continuum components are more complicated, multi-Gaussians are fitted over emission >3σ). The result is presented in Table 2. For detected sources, when a source has more than

Table 1. VLBA observations.

Galaxy	Right ascension/declination J2000	Fringe finder	Calibrator	RA/Dec uncertainty (arcsec)
Mrk 0001/NGC 0449	$01^h16^m07^s.20/+33°05'21''.75$	2007+777/3C84	J0137+3122/J0112+3208	0.02/0.02
J0126–0417	$01^h26^m01^s.64/-04°17'56''.23$	2007+777/3C84	J0123–0348	0.04/0.04
NGC 0591/Mrk 1157	$01^h33^m31^s.23/+35°40'05''.79$	2007+777/3C84	J0137+3309	0.10/0.1
Mrk 1029	$02^h17^m03^s.57/+05°17'31''.15$	2007+777/ DA193	J0215+0524	0.18/0.18
NGC 1194	$03^h03^m49^s.11/-01°06'13''.48$	2007+777/ DA193	J0259–0019	0.03 /0.03
J0350–0127	$03^h50^m00^s.35/-01°27'57''.40$	2007+777/DA193	J0351–0301	0.15/0.15
J0437+6637	$04^h37^m08^s.28/+66°37'42''.10$	2007+777/DA193	J0449+6332/J0429+6710	0.12/0.12
UGC 3193	$04^h52^m52^s.56/+03°03'25''.52$	2007+777/DA193	J0453+0128	0.11/0.29
NGC 2273	$06^h50^m08^s.69/+60°50'45''.10$	2007+777/DA193	J0638+5933	0.28/0.27
UGC 3789	$07^h19^m30^s.95/+59°21'18''.37$	3C84/4C39.25	J0737+5941	0.08/0.08
Mrk 0078	$07^h42^m41^s.73/+65°10'37''.39$	3C84/4C39.25	J0737+6430	0.03/0.03
Mrk 1210/Phoenix	$08^h04^m05^s.86/+05°06'49''.83$	DA193/4C39.25/3C345	J0803+0421	0.03/0.03
Mrk 1419/NGC 2960	$09^h40^m36^s.38/+03°34'37''.36$	3C84/4C39.25	J0930+0034	0.14/0.13
NGC 4388	$12^h25^m46^s.78/+12°39'43''.77$	DA193/4C39.25/3C345	J1225+1253	0.02/0.02
NGC5765b	$14^h50^m51^s.5/+05°06'52''.0$	DA193/4C39.25/3C345	J1458+0416	1.25/1.25
UGC 9639/Mrk 0834	$14^h58^m35^s.99/+44°53'01''.0$	4C39.25/2007+777	J1459+4442	0.5/0.5
NGC 6264	$16^h57^m16^s.13/+27°50'58''.5$	4C39.25/2007+777	J1659+2629	0.5/0.5
NGC 6323	$17^h13^m18^s.07/+43°46'56''.8$	4C39.25/2007+777	J1707+4536	0.5/0.5
Mrk 0001	$01^h16^m07^s.209/+33°05'21''.634$	3C84	J0119+3210	0.001/0.001
UGC 3193	$04^h52^m52^s.5569/+03°03'25''.768$	3C84	J0459+0229	0.001/0.001
Mrk 1210	$08^h04^m05^s.8570/+05°06'49''.846$	4C39.25/3C84	J0803+0421	0.0008/0.002
Mrk 1419	$09^h40^m36^s.3835/+03°34'37''.289$	4C39.25/3C84	J0930+0034	0.001/0.001

Notes. Column 1: name of galaxy. The sources in bold hold clean maser disks (see Sect. 2). Column 2: J2000 right ascension and declination. For NGC 5765b, NGC 6323, NGC 6264, and UGC 9639 the coordinates are taken from NED, and for the remaining sources the coordinates are from Kamali et al. (2017). Column 3: fringe finders. Column 4: phase calibrators. Column 5: right ascension and declination uncertainties. The second VLBA observations are presented in the lower part. The pointing coordinates for the second observations were taken from the first run of VLBA observations.

Table 2. Obtained properties for detected sources.

Galaxy	5 GHz peak flux (mJy beam^{-1}) First obs || Second obs	5 GHz integrated flux (mJy) First obs || Second obs	Right ascension/declination	Uncertainties (mas/mas)	α_5^{33}	T_b (K)	Putative core
Mrk 0001	1.30 ± 0.09 || 1.05 ± 0.05	8.6 ± 0.8 || 8.9 ± 0.3	$01^h16^m07^s.208/+33°05'21''.636$	0.018/0.017	0.39 ± 0.03	6.5×10^6	NW
Mrk 1210	0.92 ± 0.07 || 3.10 ± 0.07	15.05 ± 0.8 || 17.9 ± 0.7	$08^h04^m05^s.8570/+05°06'49''.848$	0.0008/0.002	0.40 ± 0.01	1.3×10^7	CN
Mrk 1419	0.94 ± 0.06 || 0.66 ± 0.03	1.7 ± 0.2 || 0.7 ± 0.3	$09^h40^m36^s.3835/+03°34'37''.289$	0.001/0.001	0.31 ± 0.09	$>2.6 \times 10^6$	…
NGC 2273	1.6 ± 0.03 || …	3.3 ± 0.1 || …	$06^h50^m08^s.6577/+60°50'44''.9012$	0.0005/0.0006	0.11 ± 0.06	9.1×10^6	…
UGC 3193	0.7 ± 0.06 || 1.3 ± 0.03	2.0 ± 0.1 || 3.0 ± 0.9	$09^h40^m36^s.3836/+03°34'37''.290$	0.0004/0.001	-0.14 ± 0.04	1.3×10^7	N

Notes. Column 1: name of galaxy. The sources in bold hold clean maser disks (see Sect. 2). Column 2: 5 GHz peak flux density of the brightest component. Column 3: 5 GHz integrated flux. For detected sources with multiple components the reported flux is the sum of the fluxes from all the components. Column 4: J2000 right ascension and declination obtained (except for NGC 2273) from the second observations for the peak position of the brightest component. Column 5: right ascension and declination uncertainties. Column 6: spectral index obtained from 33 GHz VLA observation and 5 GHz VLBA observations assuming a power law dependence of $S \propto \nu^{-\alpha}$. Column 7: brightness temperatures. If the source is unresolved, a lower limit is given. Column 8: putative core of the AGN, corresponding to the component with highest brightness temperature. NW stands for northwestern, CN for central, and N for northern.

one component, the flux reported in Table 2 is the total flux density which includes all the components[2]. For positions reported in Tables 1 and 2, the uncertainties include the statistical uncertainty, the uncertainty in the phase calibrator position or the calibrator's size if the calibrator is resolved, and the systematic errors which are estimated from $(\Psi^2 + \mathrm{beam}^2)^{1/2} \times (1/[S/N] + 1/20)$, where Ψ is the source major axis, beam is the beam size, and S/N is the signal-to-noise ratio (White et al. 1997).

[2] The radio luminosities are also obtained from the total flux densities unless mentioned otherwise.

4.1. Continuum images and previous radio observations

Here we review our maps and other radio observations available in the literature for the five detected sources.

Mrk 0001. We observed compact radio emission in our 33 GHz radio maps with a position angle (PA) of 120° ± 2°. In the *C*-band VLBA data we see extended emission, also in the northwest-southeast direction. The maser disk has a PA of 6.4°±10° and its rotation axis is by 17°±11° misaligned from the jet propagation direction. The systemic masers are not observed in this source (Kuo et al., in. prep.).

Table 3. Sample properties.

Galaxy	Distance (Mpc)	5 GHz upper limits (mJy)	rms (μJy beam^{-1}) First obs || Second obs	33 GHz flux (mJy)	Hard X-ray flux (10^{-11} erg s^{-1} cm^{-2})	log L_{H_2O} ($L_\odot$)	Type of activity
J0126-0417	76.2 ± 5.4	<0.13	42.5	0.14 ± 0.02	<0.34	2.1	*U*
J0350–0127	174.2 ± 12.2	<0.13	37.6	0.17 ± 0.04	$0.45^{+0.17}_{-0.16}$	3.7	*U*
J0437+6637	52.9 ± 3.7	<0.13	36.8	0.11 ± 0.02	0.29 ± 0.14	1.4	*U*
Mrk 0001	64.2 ± 4.5	…	45.6 || 49.7	3.97 ± 0.13	<0.32	1.9	Sy2
Mrk 0078	159.9 ± 11.2	<0.10	33.4	1.69 ± 0.11	0.63 ± 0.18	1.6	Sy2
Mrk 1029	126.0 ± 8.8	<0.11	36.7	1.29 ± 0.16	<0.35	2.8	*U*
Mrk 1210	61.3 ± 4.3	…	80.0 || 32.0	8.14 ± 0.43	3.58±0.20	2.0	Sy2, Sy1
Mrk 1419	75.3 ± 5.3	…	39.0 || 37.0	0.36 ± 0.07	<0.34	2.7	LINER
NGC 0591	61.1 ± 4.3	<0.11	41.3	1.52 ± 0.12	$0.37^{+0.12}_{-0.11}$	1.5	Sy2
NGC 1194	55.4 ± 3.9	<0.12	38.5	1.05 ± 0.04	2.21±0.18	2.8	Sy 1.9
NGC 2273	26.8 ± 1.9	…	39.7	3.04 ± 0.36	0.67 ± 0.16	0.9	Sy2
NGC 4388	40.8 ± 2.9	<0.13	44.6	3.01 ± 0.08	$15.81^{+0.16}_{-0.15}$	1.2	Sy2
NGC 5765b	122.0 ± 8.5	<0.11	37.2	…	$0.40^{+0.17}_{-0.18}$	3.6	*U*
NGC 6264	145.4 ± 10.2	<0.12	38.5	…	<0.32	3.1	Sy2
NGC 6323	110.6 ± 7.8	<0.12	39.1	…	<0.30	2.7	Sy2
UGC 3193	63.2 ± 4.4	…	31.3 || 34.0	0.80 ± 0.05	<0.39	2.5	*U*
UGC 3789	47.4 ± 3.3	<0.11	35.0	0.20 ± 0.02	$0.26^{+0.14}_{-0.13}$	2.7	Sy2
UGC 9639	155.9 ± 10.9	<0.09	30.0	…	<0.26	2.6	LINER

Notes. Column 1: name of galaxy. The sources in bold hold clean maser disks (see Sect. 2). Column 2: Hubble flow distances (relative to the 3 K Cosmic Microwave Background) in Mpc, assuming $H_0 = 70\,\mathrm{km\,s^{-1}\,Mpc^{-1}}$ (see Sect. 2). Column 3: 3σ upper limit for the non-detections in the VLBA 5 GHz observations. Column 4: rms of the 5 GHz maps. Column 5: 33 GHz integrated flux densities with uncertainties (Kamali et al. 2017). Column 6: *Swift*/BAT hard X-ray fluxes (20–100 keV) with uncertainties (Litzinger et al., in prep.). Column 7: logarithm of water maser luminosity in units of solar luminosity (Zhang et al. 2012, modified for $H_0 = 70\,\mathrm{km\,s^{-1}\,Mpc^{-1}}$). The NGC 5765b and UGC 9639 data are from Kuo et al. (2018). Column 8: types of nuclear activity following NED; *U* stands for unidentified.

Table 4. Position angles (PAs).

Galaxy	Maser disk (°)	5 GHz jet direction (°)	Jet offset (°)	33 GHz continuum (°)	Galaxy scale (°)	Ref.
Mrk 0001	6.4 ± 10	113 ± 5	17 ± 11	120 ± 2	77.5	1
Mrk 1210	62.58 ± 0.45	127 ± 22	26 ± 22	179 ± 83	160.0	2
Mrk 1419	49 ± 0.7	159 ± 2	20 ± 1	117 ± 84	40.2	3
NGC 2273	153 ± 4.6	95 ± 1	32 ± 5	83 ± 3	63.3	3
UGC 3193	–	175 ± 0.2	–	167 ± 4	177.4	–

Notes. Column 1: name of galaxy. The sources in bold hold clean maser disks (see Sect. 2). Column 2: maser disk PAs and their uncertainties. Column 3: jet propagation direction, obtained from a linear fit on the position of the flux maxima in multicomponent sources (see Sect 5.1). If there is only one component, the 5 GHz continuum PA of this component represents the jet propagation direction. Column 4: PA difference between the disk rotation axis (the normal vector to the disk) and jet propagation direction and the uncertainties. Column 5: 33 GHz larger scale PAs from Kamali et al. (2017). Column 6: large-scale galactic disk PA from HyperLeda. Column 7: references for maser disk PA. (1) Kuo et al. (in prep.); (2) Zhao et al. (2018); (3) Kuo et al. (2011).

Mrk 1210. As mentioned before, four of our VLBA detected sources were re-observed to obtain higher S/N values. While morphologies are very similar for three sources in both observations, for Mrk 1210 the southeastern component was not detected in the data set from the first observations and the northwestern extended emission is less prominent in this data, likely due to insufficient sensitivities. A former 6 cm VLBA observation of this galaxy has shown a structure similar to those found in our re-observations, which is shown in Fig. 1, except that the northwestern component is resolved into four subcomponents (Middelberg et al. 2004). The flux reported by Middelberg et al. (2004) for the central component in Fig. 1 is the same as in our observations (5 mJy). However, the flux reported for the northwestern component is less than ours (9.1 ± 1.1 mJy compared to 13.7 ± 0.4 mJy). The southeastern component is considered a tentative detection in the work of Middelberg et al. (2004) and therefore no flux is reported for this component. Identifying the core of the galaxy the jet is emanating from is not easy since both northwestern and central components have steep spectra. Middelberg et al. (2004) reported a spectral index of $\alpha^{18\,\mathrm{cm}}_{6\,\mathrm{cm}} = 1.26$ for the northwestern and $\alpha^{18\,\mathrm{cm}}_{6\,\mathrm{cm}} = 0.78$ for the central component obtained from VLBI observations with matching beam sizes using the $S \propto \nu^{-\alpha}$ convention. The maser configuration is consistent with a rotating disk. However, only one single maser component is detected at the systemic velocity of the galaxy. The high velocity masers also deviate slightly from an edge-on, flat, Keplerian disk model. This implies that if the masers arise from a disk, its inclination is deviating ~10° from an edge-on disk (inclination = $100.68^{+1.13\,\circ}_{-0.90}$), and there is potential warping or eccentricity in the disk (Zhao et al. 2018). Mrk 1210

shows long-term variability in the X-rays and has changed from Compton-thick to Compton-thin over a period of approximately 17 years (Masini et al. 2017). This variability was interpreted as a combination of the intrinsic variability of the AGN and presence of an obscuring cloud passing through the line of sight.

Mrk 1419. This galaxy poses a clean maser disk (Kuo et al. 2011). Sun et al. (2013) reported extended emission with a PA of 125° ± 10° from 20 cm radio data. In our VLA maps we see a weak extension in the southeast-northwest direction with a PA of 117° ± 84°. Gaussian deconvolution of our 5 GHz map shows a compact component that is not clearly resolved and may contain a weak extension with a PA of 159° ± 2°. The outer part of the maser disk shows some degree of warping (Kuo et al. 2011).

NGC 2273. This galaxy poses a clean maser disk (Kuo et al. 2011). NGC 2273 was previously observed with the VLBA at *C* band in 2004 by Lal et al. (2004) and showed a compact radio core. Anderson & Ulvestad (2005) observed this galaxy at 8.4 GHz with the VLBA and detected radio emission extended along the northwest to southeast direction with a beam width of approximately 2 mas × 1 mas. The structure is similar to our map shown in the lower right panel of Fig. 1. The distribution of the masers shows a hint of a warp in the disk (Kuo et al. 2011).

UGC 3193. In our 33 GHz data, we see extended emission in the north-south direction, the same as we observe in the *C*-band VLBA data. The southern component is not resolved in the Gaussian deconvolution. The maser disk orientation and position is not yet known for UGC 3193.

4.2. A note on the non-detections

About 72% of the sources in our original sample of 18 sources were not detected. Considering that ~70% of the undetected sources were previously detected in our VLA observations and assuming a flat spectrum or rising flux densities with decreasing frequency, we might expect to detect these sources in the VLBA observations. Figure 2 shows the expected flux at 5 GHz (assuming a flat spectrum) and the 5 × rms noise of our VLBA maps (for a 5σ detection limit of a single spatially unresolved continuum component). The five detected sources are among the brightest ones as shown in Fig. 2. However, there are similarly bright sources among the undetected ones. Either these sources have inverted spectra, or extended emission is resolved out. Time variability of AGNs is another issue that could affect the detection rates. We searched for trends of common properties among the detected sources, such as X-ray, IR, radio, or maser luminosity limits, but did not succeed in finding any. We report 3σ upper limits for the undetected sources, rms of our maps, as well as hard X-ray and 33 GHz fluxes in Table 3.

5. Discussion

5.1. Orientation of the jets with respect to the maser disks

In NGC 4258, the prototypical H_2O megamaser galaxy, the rotation axis of the maser disk is aligned with the inner part of the extended jet (Cecil et al. 1992). Here we focus on identifying the orientation of the jet with respect to that of the maser disk in our sample. Once again we note that two of the detected sources, Mrk 1419 and NGC 2273, are among the clean maser disks (see Sect. 2), while the other three detected galaxies, Mrk 0001, Mrk 1210, and UGC 3193, are among those exhibiting a non-clean disk, i.e., the masers might arise from either disks or outflows. In the following discussion, we consider the possibility

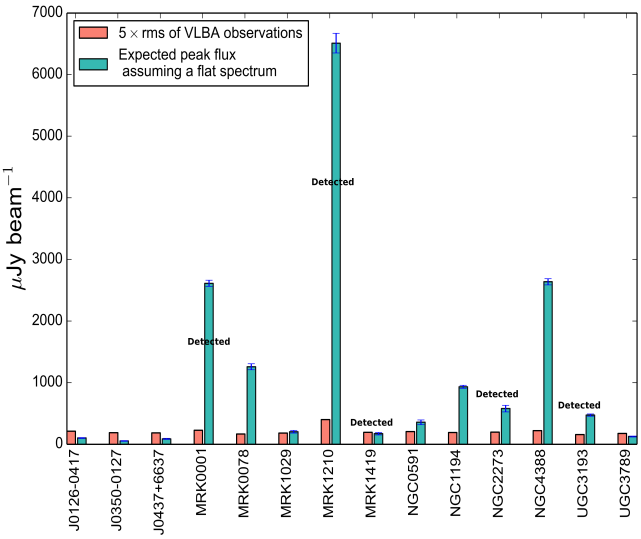

Fig. 2. Expected flux densities in the case of a flat radio spectrum compared to the rms noise of the maps. The five detected sources are labeled.

that the masers arise from the circumnuclear disk surrounding the SMBHs[3]. Then for four out of the five detected galaxies in our sample, Mrk 0001, Mrk 1210, Mrk 1419, and NGC 2273, the maser disk orientation is known (see Sect. 4 for more information). As mentioned before, in our sample the maser disk is viewed edge-on (±10°) and the normal vector to the disk is in the plane of the sky. We do not apply any inclination corrections to the measured PAs. Instead we assume that the PA (measured east of north) of the radio continuum shows the PA of the elongation of the jet. If more than one component is detected, we assume that a line going through the central position of each component (obtained from Gaussian fits) represents the jet propagation direction. The same convention for measuring the PAs (east of north) is used for all other reported PAs.

For all four sources, the jets are misaligned with respect to the normal vector to the maser disk. However, they are confined to a cone within ~0.6 radians (32°) of the disks' normal. Table 4 presents PAs obtained in this work and from the literature, and Fig. 3 shows a comparison between the PAs of different scale disks and the radio continuum. For the null hypothesis that the jets have random distribution in space, the probability that we observe these four measured PA offsets is 0.009, indicating that the jet orientations are not random with a 99.1% confidence level (see Appendix A for more details). On the other hand, the PA offset may be related to the outer and inner radii of the disk: the larger the disk size, the smaller the offset (see Figs. 4 and 5). We note, however, that our conclusion is based on a sample of four sources only (where two of them are non-clean disks), so that a study of a larger sample is needed to verify or falsify our finding.

5.2. Multiscale position angle

The PAs of disks on different scales are available for three of the VLBA-detected sources (Greene et al. 2013; Pjanka et al. 2017). Therefore, we can compare the alignment of the jet with the angular momentum orientation of the disks on different scales. Our VLBA radio continuum in Mrk 1210 is misaligned by ~26° with the maser disk's normal. However, it is misaligned with the nuclear region of the galaxy (with size of 170 pc) by only

[3] For clarity, clean maser disks and non-clean maser disks are shown with different markers in our plots.

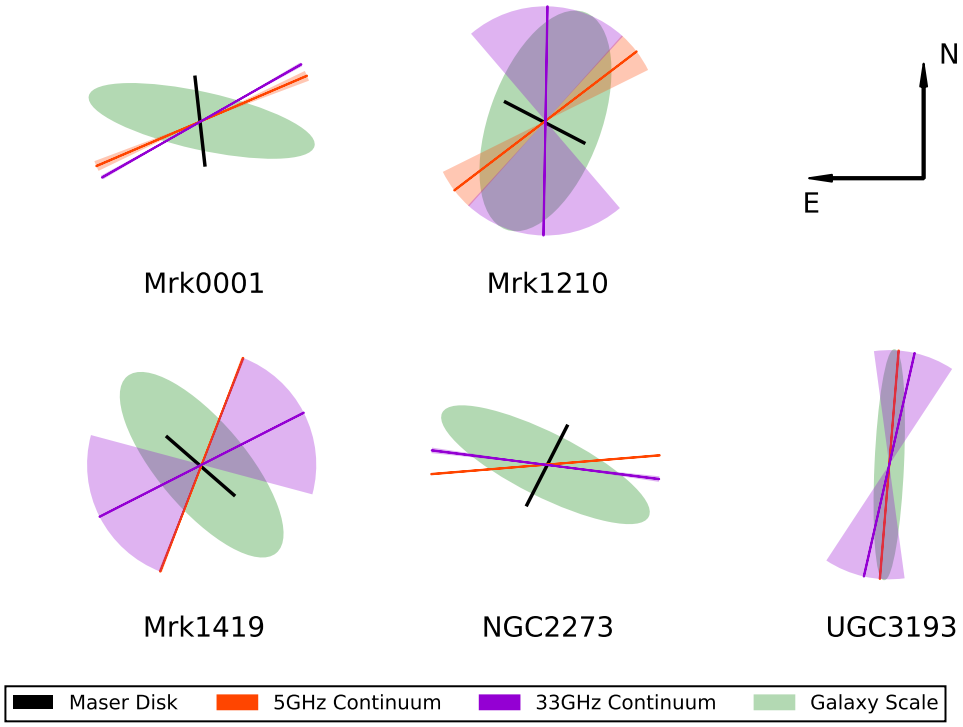

Fig. 3. Position angles (PAs) on different scales. The galaxy scale PA is shown as a green ellipse. The minor axis of the ellipse represents the inclination of the galaxy, i.e., the broader the minor axis, the lower the inclination. The 5 GHz VLBA and 33 GHz VLA radio continuum PAs are shown with orange and violet solid lines, respectively, and the uncertainties on the PA of the radio continuum are shown as shaded wedges. The maser disk is shown as a black solid line. For UGC 3193 detailed maser images are not yet available. The sizes of the ellipses, lines, and wedges do not represent correct relative scales.

~8°. The radio continuum orientation is displaced by ~57° from the angular momentum orientation of the large-scale disk. For NGC 2273, the VLBA radio continuum is not aligned with any of the rotation axes: ~32° from the maser disk's normal, ~36° from the angular momentum orientation of the nuclear 150 pc scale disk, and ~58° from the normal vector to the galaxy's large-scale disk. In Mrk 1419, which has likely experienced a merger or some interaction (Läsker et al. 2016), the maser disk and the nuclear region with a size of 270 pc are aligned and the jet is ~20° from the angular momentum direction of this disk, while the galaxy's large-scale disk has a normal vector that is ~29° away from the jet direction.

5.3. Radio continuum positions relative to the maser positions

Compact radio emission is detected in the nuclei of most galaxies (Herrnstein et al. 1997, and references therein). Since the centers of the maser disks are the gravitational centers of the nuclear regions, we expect the centers of the maser disks to coincide with their radio continuum core representing the nucleus of the galaxy. For three sources among the detected ones, Mrk 0001, Mrk 1419, and NGC 2273, the maser positions are available. For our radio continuum data the central position from the Gaussian fit of the component with the highest brightness temperature (if there is more than one) is considered as the position of the nuclear source (see Sect. 5.4). In Table 5 we present the spatial offsets of the maser disk with respect to the radio continuum. For Mrk 1419 and NGC 2273, the maser positions are from VLA observations. Within the uncertainties, the maser positions for all three sources are consistent with those of the radio continuum. For Mrk 0001, however, in our second observations the phase calibrator was resolved with a major axis of ~15 mas and therefore we report the position offset with respect to the continuum position in our first observations which has a higher position accuracy. The proper motion of the galaxies can be neglected. In the case of a speed of 1000 km s^{-1} in the plane of the sky and a distance D = 50 Mpc, the expected shift is only 4 μarcsec yr^{-1}.

5.4. Spectral indices and brightness temperatures

We obtained the spectral indices for the detected sources between 33 GHz and 5 GHz. They are presented in Table 2. The indices were obtained assuming a power-law dependence for the fluxes ($S \propto \nu^{-\alpha}$). We should note that the VLA observations have linear beam sizes about 100 times those of the VLBA observations. The spectral indices have a mean of $\alpha = 0.21 \pm 0.20$.

We also obtained the brightness temperatures (T_B), using

$$T_b = \frac{2\ln(2)}{k_B\,\pi}\,\frac{\lambda^2\,S_{tot}}{\theta_{maj}\,\theta_{min}}, \quad (1)$$

where k_B is the Boltzmann constant, S_{tot} is the total flux density, λ is the wavelength of observation, and θ_{maj} and θ_{min} are the deconvolved sizes of the major and minor axes of the source. When the component is unresolved, the beam size is used as an upper-limit for the source size. Therefore, the corresponding T_B is a lower limit. The obtained brightness temperatures are listed in Table 2. For sources with more than one component, we give the measurement for the component with highest T_b, which we identify as the putative core of the AGN. It should be noted that we do not know the spectral indices for the individual components; therefore, the brightness temperature is the only

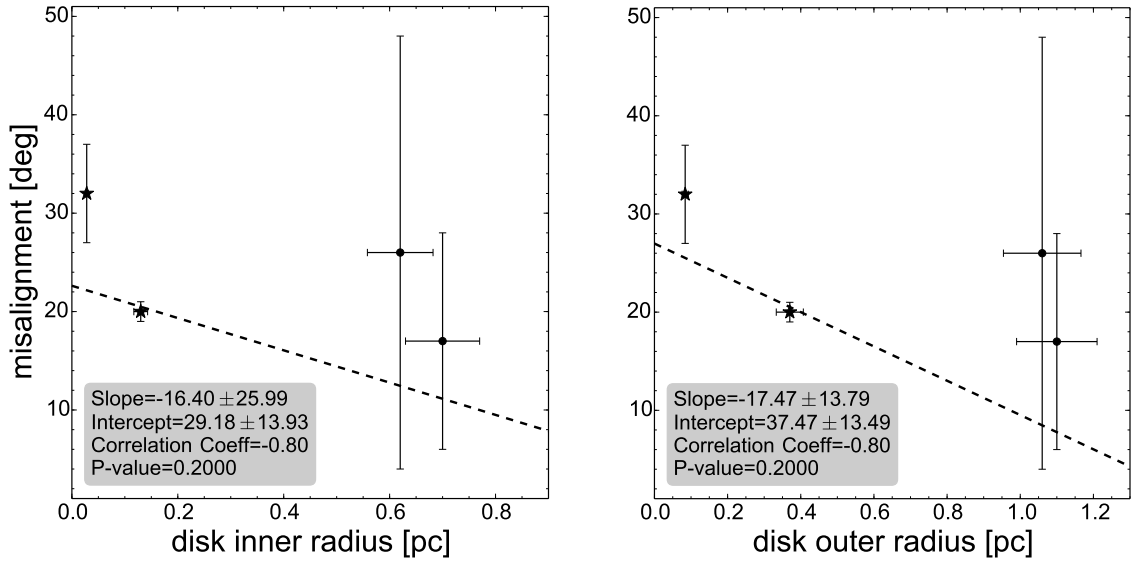

Fig. 4. Misalignment of the jet and the normal to the maser disk versus inner (*left panel*) and outer (*right panel*) radius of the maser disk. The clean maser disks are shown as stars and the non-clean disks as dots.

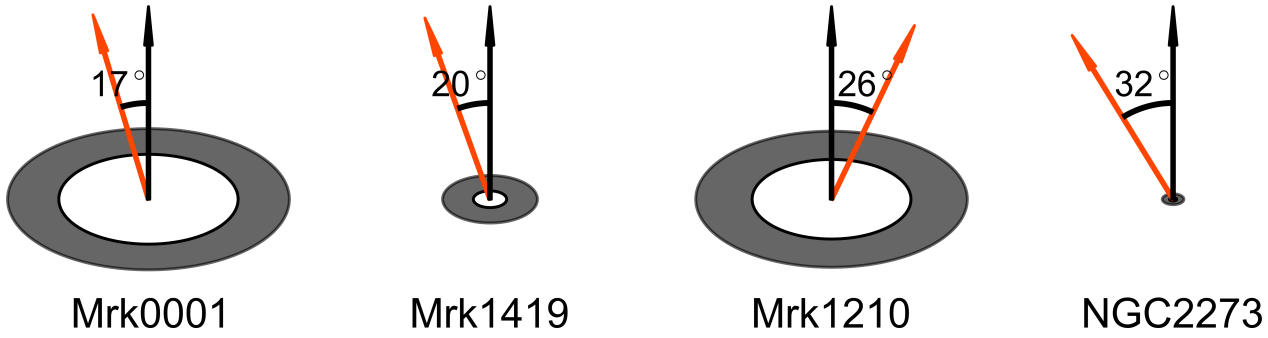

Fig. 5. Misalignment of the jet (orange arrow) and the rotation axis (black arrow) of the maser disk (see also Table 4). The disk sizes are to scale with respect to each other.

Table 5. Separation of the maser disk from the continuum sources.

Galaxy	δ RA (mas)	δ Dec (mas)	Reference
Mrk 0001	4.5 ± 1.0	0.4 ± 1.0	1
Mrk 1419	1.5 ± 10.0	1.5 ± 10.0	2
NGC 2273	22.5 ± 10.0	3.3 ± 10.0	2

Notes. Column 1: name of galaxy. Columns 2 and 3: separation of the maser disk from the center of the 5 GHz nuclear continuum source and the uncertainties. For Mrk 0001 the separation is for our first observation and with respect to the continuum source in the northwest of the image. Column 4: references for maser disk positions. (1) Kuo et al., in prep.; (2) Kuo et al. (2011).

tool that can tentatively define the AGN's core. All sources have $T_B > 10^6$, consistent with non-thermal emission.

5.5. Radio luminosity versus other properties of the galaxies

5.5.1. Radio luminosity versus X-ray luminosity and the SMBH mass: fundamental plane of black hole activity

The fundamental plane (FP) of black hole activity is an empirical relation between the radio continuum luminosity, X-ray luminosity, and black hole (BH) mass. This relation holds for 10 orders of magnitude in radio luminosity and ranges from stellar mass BHs (in X-ray binaries) to SMBHs, supporting the idea that jet physics is scale invariant (Merloni et al. 2003). For many years there have been efforts to understand the accretion mechanism in the SMBHs and how the accretion rate is related to the SMBH mass and the radio and X-ray luminosities. Studies have suggested that the radio luminosity depends on both SMBH mass and accretion rate of material onto the black hole (Falcke & Biermann 1995). The SMBH mass can be determined observationally, and the accretion rate can be inferred through measuring the luminosity at those frequencies at which the accretion process dominates. For example, the accretion flow can be inferred from the X-ray luminosity since the X-ray emission is produced by the accretion of material onto the SMBHs. The scaling of the X-ray luminosity with the accretion rate depends on the physics of the disk, e.g., whether it is radiatively efficient or not (a quantitative description of these models is beyond the scope of this paper; see Merloni et al. 2003, and references therein). The X-ray emission could also be produced by the inverse Compton effect involving synchrotron radiation. In summary, we expect the core radio luminosity to be correlated with the X-ray luminosity and also with the black hole mass.

The following plane equation describes the FP of BH activity

$$\log L_R\,(\mathrm{erg\,s^{-1}}) = \xi_X \log L_X\,(\mathrm{erg\,s^{-1}}) + \xi_M \log M\,[M_\odot] + b_R, \quad (2)$$

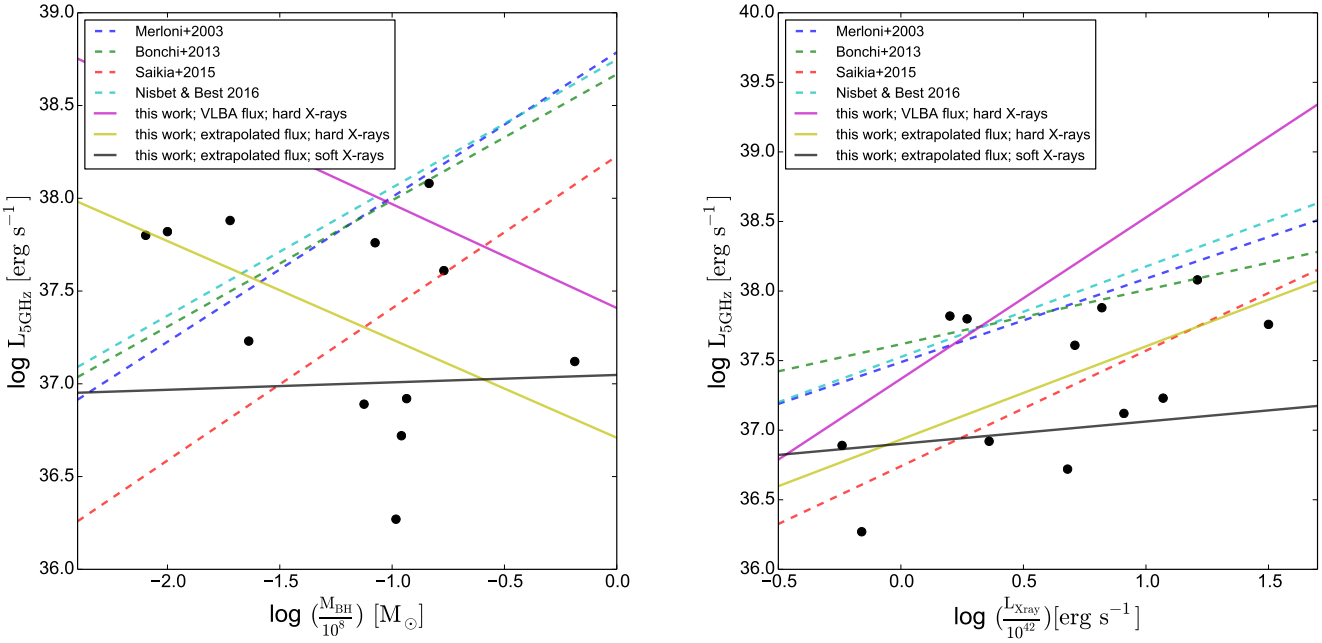

Fig. 6. Parameters of the fundamental plane of the black hole activity. *Left panel*: 5 GHz radio luminosity versus black hole mass. The data points are the extrapolated 5 GHz fluxes obtained from the 33 GHz data (Kamali et al. 2017), using a spectral index of 0.21 (see Sect. 5.5.1). Dashed lines represent ξ_M available in the literature (see Eq. (2)), assuming a constant X-ray luminosity (mean value of our data) and the solid lines represent ξ_M obtained in this work. *Right panel*: 5 GHz radio luminosity versus X-ray luminosity. Dashed lines represent ξ_X available in the literature, assuming a constant black hole mass (mean value of our data) and the solid lines represent ξ_X obtained in this work.

where L_R, L_X, and M are the radio luminosity, X-ray luminosity, and the BH mass, respectively; b_R is the zero intercept; and ξ_X and ξ_M are the linear regression coefficients. The coefficients in Eq. (2) depend on the accretion efficiency, electron spectral index, viscosity of the disk and initial conditions at the base of the jet such as dependence of magnetic energy density on the SMBH mass and accretion rate. Others have followed the lead of Merloni et al. (2003) and investigated the FP using different subsamples (e.g., Saikia et al. 2015; Körding et al. 2006; Gültekin et al. 2009; Bonchi et al. 2013; Nisbet & Best 2016). All these studies fit similar coefficients, which is somewhat surprising since the SMBH mass determinations differ from sample to sample. We note that a sample for which accurate BH mass measurements have been obtained from edge-on megamaser disks has not yet been analyzed.

Adopting X-ray luminosities from Litzinger et al. (in prep.), obtained using data from the *Swift*/BAT instrument in a range of 20–100 keV (see Table 3), the black hole masses from the MCP and radio luminosities from this work, we fitted the same function to our data using the least-squares method. The fitting parameters are shown in the first row of Table 6. We considered increasing the number of sources for this analysis by extrapolating the 5 GHz luminosities from the 33 GHz radio luminosities, using the mean of the indices between our 33 GHz and 5 GHz observations (see Table 2). This sample with extrapolated fluxes includes 12 sources that have known SMBH masses. The result of the fit is presented in the second row of Table 6. We should note that the mentioned studies that probe the FP use soft X-ray data (2–10 keV) and this can cause a discrepancy with our result. We also tried to fit Eq. (2) to a sample of five sources for which we have soft X-ray data (Masini et al. 2016) and extrapolated 5 GHz fluxes. The fitting parameters are shown in the third row of Table 6. We present the fitting parameters for the FP in Fig. 6. A selection of parameters reported in the literature is also presented with dashed lines. As seen in Fig. 6, in our sample the black hole mass decreases with increasing radio luminosity. This is opposite to what is found in other studies and could be responsible for the significant difference between this work and other studies for the obtained value of ξ_M. On the other hand, galaxies with H_2O megamaser disks may not follow the well-known scaling relation between the BH mass and the stellar dispersion velocity of the galaxies. They may show an offset with respect to the early-type galaxies, while other spiral galaxies with non-maser dynamically determined BH masses do not show such an offset (Greene et al. 2016), perhaps because the maser disks are preferentially formed in spirals with particularly low mass nuclear sources or because the non-maser dynamical measurements are missing the low mass end of the BH distribution due to their too small spheres of influence. It should be noted that these interpretations are only two of the possible scenarios available.

5.5.2. Radio luminosity versus [OIII] luminosity

Previous studies have shown a strong correlation between the optical narrow emission-line luminosity and the radio luminosity of radio galaxies (e.g., Baum & Heckman 1989; Rawlings & Saunders 1991). This correlation is valid over four to five orders of magnitude for both radio and line luminosities, and could be the result of a common energy source for optical line and radio emissions, suggesting that the luminosity depends on the properties of the central engine. It is also possible that both optical line and radio luminosities depend on a third parameter, e.g., the amount of cold gas present on kpc scales (Baum & Heckman 1989). A correlation was reported by Baum & Heckman (1989) between the Hα+[N II] line luminosity, $L_{\rm line}$, and total radio luminosity at the VLA scales for a sample of radio galaxies, where $L_{\rm line}$ is proportional to $L_{\rm radio}^{0.73}$. Other studies have compared the radio core luminosity and the luminosities from the narrow line region, where the core is defined as the unresolved component with highest flux density in the radio

Table 6. Fit parameters of fundamental plane for black hole activity.

ξ_X	ξ_M	b_R	Notes
1.16 ± 1.11	-0.56 ± 0.97	-7.61 ± 45.13	This work, hard X-rays, 5 GHz VLBA fluxes, 5 sources
0.67 ± 0.20	-0.53 ± 0.19	12.27 ± 8.18	This work, hard X-rays, extrapolated 5 GHz fluxes using $\alpha = 0.21$, 12 sources
0.16 ± 3.3	0.04 ± 5.6	30.1 ± 141	This work, soft X-rays, extrapolated 5 GHz fluxes using $\alpha = 0.21$, 5 sources

Notes. Column 1: coefficient of X-ray luminosity in Eq. (2). Column 2: coefficient of SMBH masses in Eq. (2). Column 3: intercept of Eq. (2). Column 4: extrapolated 5 GHz fluxes are obtained using spectral index 0.21 between 33 GHz VLA observation and 5 GHz VLBA observations assuming a power-law dependence of $S \propto \nu^{-\alpha}$.

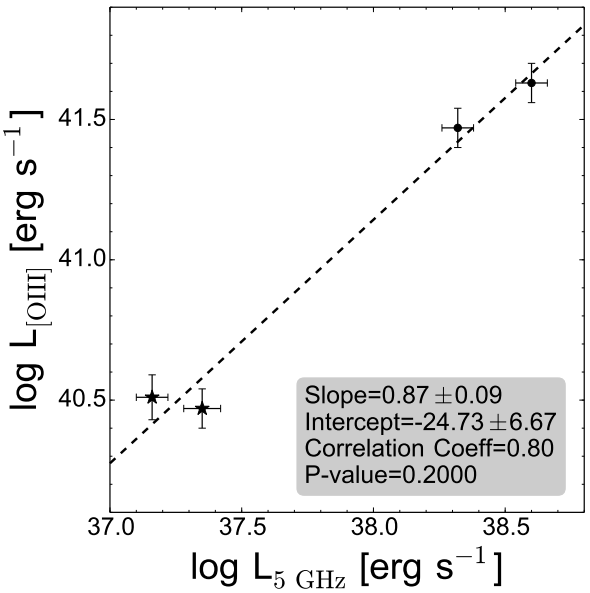

Fig. 7. 5007 Å [OIII] versus 5 GHz luminosity. The slope and the intercept of the fitted line, correlation coefficient, and the P-value of the rank correlation test are shown in the plot. The clean maser disks are shown as stars and the non-clean disks as dots.

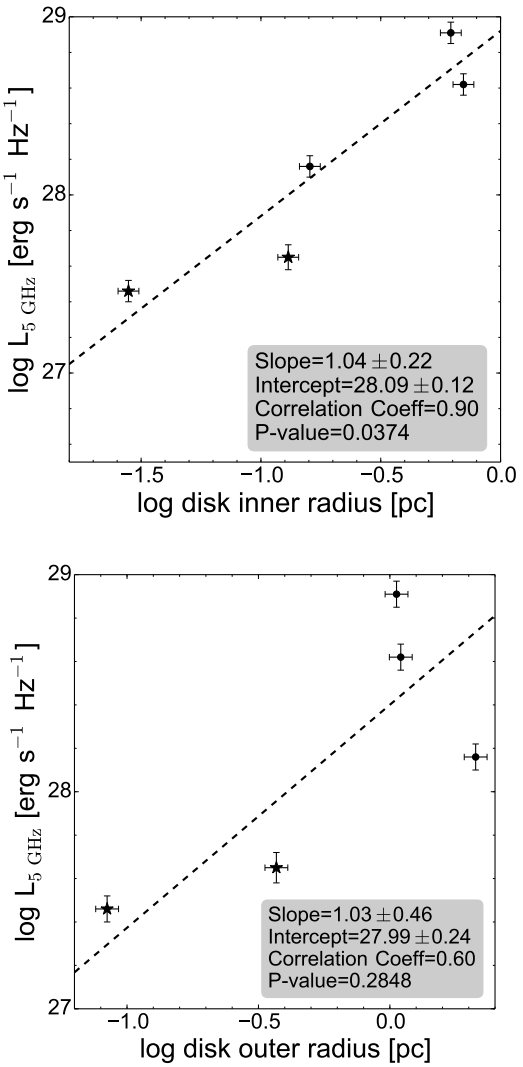

Fig. 8. 5 GHz luminosities versus the inner radius (*upper panel*) and the outer radius (*lower panel*) of the maser disk. The slope and the intercept of the fitted line, correlation coefficient, and the P-value of the rank correlation test are shown in the plot. The clean maser disks are shown as stars and the non-clean disks as dots.

observations. Buttiglione et al. (2010) reported $L_{[OIII]} \propto L_{core}^{0.75}$ for a sample of high excitation galaxies and Baldi et al. (2018) reported $L_{[OIII]} \propto L_{core}^{0.35\pm0.20}$ for a sample of LINER galaxies. Therefore, we checked for a possible linear correlation between the optical emission-line luminosities and radio luminosities in our sample. We obtained the 5007 Å[OIII] luminosities from NED taken by the SDSS. Four of our five detected sources, Mrk 0001, Mrk 1210, Mrk 1419, and NGC 2273, have [OIII] luminosities. Using a Spearman rank correlation test, we find a correlation between 5 GHz (derived from VLBI) and the [OIII] luminosities, $L_{[OIII]} \propto L_{5\,GHz}^{0.87\pm0.09}$. The correlation coefficient is 0.80, and the P-value, indicating that the likelihood that parameters are unrelated, is 0.2 (see Fig. 7). While this suggests reasonable agreement with previously mentioned studies, we note that the result is based on very few sources. We also note that the correlation of radio luminosity with emission-line luminosity extends over five orders of magnitude in L_{radio} and four orders of magnitude in L_{line}, i.e., there is ∼one order of magnitude scatter in the radio luminosity for a given line luminosity, suggesting that other criteria such as environment or different accretion modes play a role in determining the radio and optical emission-line luminosities of these galaxies (Baum & Heckman 1989).

5.5.3. Radio luminosity versus maser disk radius

In our pilot project (Kamali et al. 2017) we demonstrated a correlation between the disk's inner and outer radii and the 33 GHz radio luminosity of galaxies with H_2O masers in their nuclear disks (i.e., both inner and outer radii of the disk increase as the radio luminosity increases). In this work, we find a similar correlation for inner and outer disk radius versus the 5 GHz luminosities (Fig. 8). Correlations between the maser disk size and luminosity at other frequencies were investigated previously. For example, Gao et al. (2017) reported a correlation between the infrared (IR) luminosity and the maser disk's outer radius. This correlation exists because the gas temperature should be

higher than the minimum kinetic temperature of ~400 K for masing to occur. The H_2O molecules are mixed with dust and the dust temperature depends on the bolometric luminosity. Therefore, the outer radius of the maser disk also depends on the bolometric luminosity of the AGN. In Sect. 5.5.2 we showed a correlation between the 5 GHz luminosity and the [OIII] luminosity (which is a proxy for the AGN's bolometric luminosity; e.g., Bassani et al. 1999; Heckman et al. 2005). Thus, a correlation between the outer radius of the maser disk and 5 GHz luminosities is expected. Furthermore, the pressure outside the outer disk is lower than the critical pressure, which permits the molecules to exist (Neufeld et al. 1994), and this critical pressure depends on the X-ray luminosity (for a detailed analysis, see Neufeld & Maloney 1995). Although a correlation between the X-ray luminosity and the maser disk size is expected, former studies did not find such a correlation (Kamali et al. 2017). High energy electrons are responsible for both synchrotron radio emission and the synchrotron self-Compton X-ray radiation (Falcke & Biermann 1995). However, our sources are Compton thick and an incorrect estimate of the column densities can affect the estimation of the intrinsic unobscured X-ray luminosities. Radio emission does not suffer from extinction and might be a better tool for estimating the impact of these high energy electrons that are confining the disk.

6. Summary

We observed a sample of 18 LLAGNs with the VLBA at *C* band (6 cm) and detected five sources: Mrk 0001, Mrk 1210, Mrk 1419, NGC 2273, and UGC 3193. We measured the orientations of the putative jets with respect to those of the maser disks. The maser disk orientation is known for all the detected sources, except for UGC 3193. All four sources have jet directions that are misaligned with the disk's normal by <0.6 radian. For the null hypothesis that the jets have random distribution in space, the probability that all four sources have a misalignment of less than 0.6 radian is 0.009, indicating that the jet orientations are not random. The PA differences seem to be related to the disk size: the larger the disk size, the more aligned the radio continuum is to the disk's normal. A tight correlation with correlation coefficient of 0.87 is observed between the 5007 Å[OIII] line luminosity and the 5 GHz radio continuum luminosity. The disk's inner and outer radii show a linear correlation with the 5 GHz continuum luminosity: the larger the inner radius of the maser disk, the brighter the central region of the galaxy at 5 GHz. We note, however, that all these results are based on a very small sample of sources. Further observations and maps of maser disks and of the nuclear regions of maser host galaxies will provide a larger sample for a more detailed investigation on the alignment of the accretion disk and jets in the galaxies where both phenomena are directly observable.

Acknowledgements. F.K. would like to thank the anonymous referee for the critical and constructive feedback. F.K. is also grateful to Gisela Noemi Ortiz-Leon for her constructive comments and discussions on the data reduction process. This work made use of the NASA/IPAC extragalactic Database (NED), which is operated by the Jet Propulsion Laboratory, California Institute of Technology, under contract with NASA. We further acknowledge the use of the Kapteyn Package (Terlouw & Vogelaar 2015), the HyperLeda database (http://leda.univ-lyon1.fr), and the SAO/NASA ADS Astronomy Abstract Service (http://adsabs.harvard.edu) and the National Radio Astronomy Observatory, which is a facility of the National Science Foundation operated under cooperative agreement by Associated Universities, Inc.

References

Anderson, J. M., & Ulvestad, J. S. 2005, ApJ, 627, 674
Baldi, R. D., Williams, D. R. A., McHardy, I. M., et al. 2018, MNRAS, 476, 3478
Bassani, L., Dadina, M., Maiolino, R., et al. 1999, ApJS, 121, 473
Baum, S. A., & Heckman, T. 1989, ApJ, 336, 702
Bonchi, A., La Franca, F., Melini, G., Bongiorno, A., & Fiore, F. 2013, MNRAS, 429, 1970
Braatz, J. A., Reid, M. J., Humphreys, E. M. L., et al. 2010, ApJ, 718, 657
Buttiglione, S., Capetti, A., Celotti, A., et al. 2010, A&A, 509, A6
Cecil, G., Wilson, A. S., & Tully, R. B. 1992, ApJ, 390, 365
Falcke, H., & Biermann, P. L. 1995, A&A, 293, 665
Gao, F., Braatz, J. A., Reid, M. J., et al. 2017, ApJ, 834, 52
Greene, J. E., Peng, C. Y., Kim, M., et al. 2010, ApJ, 721, 26
Greene, J. E., Seth, A., den Brok, M., et al. 2013, ApJ, 771, 121
Greene, J. E., Seth, A., Kim, M., et al. 2016, ApJ, 826, L32
Greenhill, L. J., Jiang, D. R., Moran, J. M., et al. 1995, ApJ, 440, 619
Gültekin, K., Cackett, E. M., Miller, J. M., et al. 2009, ApJ, 706, 404
Heckman, T. M., Ptak, A., Hornschemeier, A., & Kauffmann, G. 2005, ApJ, 634, 161
Herrnstein, J. R., Moran, J. M., Greenhill, L. J., et al. 1997, ApJ, 475, L17
Herrnstein, J. R., Moran, J. M., Greenhill, L. J., et al. 1999, Nature, 400, 539
Kamali, F., Henkel, C., Brunthaler, A., et al. 2017, A&A, 605, A84
Körding, E., Falcke, H., & Corbel, S. 2006, A&A, 456, 439
Kuo, C. Y., Braatz, J. A., Condon, J. J., et al. 2011, ApJ, 727, 20
Kuo, C. Y., Braatz, J. A., Reid, M. J., et al. 2013, ApJ, 767, 155
Kuo, C. Y., Constantin, A., Braatz, J. A., et al. 2018, ApJ, 860, 169
Lal, D. V., Shastri, P., & Gabuzda, D. C. 2004, A&A, 425, 99
Läsker, R., Greene, J. E., Seth, A., et al. 2016, ApJ, 825, 3
Masini, A., Comastri, A., Baloković, M., et al. 2016, A&A, 589, A59
Masini, A., Comastri, A., Puccetti, S., et al. 2017, A&A, 597, A100
Merloni, A., Heinz, S., & di Matteo, T. 2003, MNRAS, 345, 1057
Middelberg, E., Roy, A. L., Nagar, N. M., et al. 2004, A&A, 417, 925
Miyoshi, M., Moran, J., Herrnstein, J., et al. 1995, Nature, 373, 127
Nagar, N. M., & Wilson, A. S. 1999, ApJ, 516, 97
Nakai, N., Inoue, M., & Miyoshi, M. 1993, Nature, 361, 45
Neufeld, D. A., & Maloney, P. R. 1995, ApJ, 447, L17
Neufeld, D. A., Maloney, P. R., & Conger, S. 1994, ApJ, 436, L127
Nisbet, D. M., & Best, P. N. 2016, MNRAS, 455, 2551
Pesce, D. W., Braatz, J. A., Condon, J. J., et al. 2015, ApJ, 810, 65
Pjanka, P., Greene, J. E., Seth, A. C., et al. 2017, ApJ, 844, 165
Pringle, J. E., Antonucci, R. R. J., Clarke, C. J., et al. 1999, ApJ, 526, L9
Rawlings, S., & Saunders, R. 1991, Nature, 349, 138
Reid, M. J., Braatz, J. A., Condon, J. J., et al. 2009, ApJ, 695, 287
Reid, M. J., Braatz, J. A., Condon, J. J., et al. 2013, ApJ, 767, 154
Saikia, P., Körding, E., & Falcke, H. 2015, MNRAS, 450, 2317
Schmitt, H. R., Pringle, J. E., Clarke, C. J., & Kinney, A. L. 2002, ApJ, 575, 150
Sun, A.-L., Greene, J. E., Impellizzeri, C. M. V., et al. 2013, ApJ, 778, 47
Terlouw, J. P., & Vogelaar, M. G. R. 2015, Kapteyn Package, version 2.3, Kapteyn Astronomical Institute, Groningen, available from http://www.astro.rug.nl/software/kapteyn/
White, R. L., Becker, R. H., Helfand, D. J., & Gregg, M. D. 1997, ApJ, 475, 479
Zhang, J. S., Henkel, C., Guo, Q., & Wang, J. 2012, A&A, 538, A152
Zhao, W., Braatz, J. A., Condon, J. J., et al. 2018, ApJ, 854, 124

Appendix A: Probability distribution of the observed PA offsets

Detectable maser disks are edge-on so their normal lies in the plane of the sky. For the null hypothesis that jets have an isotropic distribution of orientations in space, what is the probability distribution $\rho(\delta)$ of the observed (projected onto the sky) PA offsets δ where $0 < \delta < \pi/2$? Let ϕ be the magnitude of the polar angle between the jet and the normal to the disk. Let θ be the azimuth angle in the disk plane, where $\theta = 0$ corresponds to the line from the disk center pointing away from the observer. Thus, $\delta = \phi \sin(\theta)$. The differential probability of observing δ for a given ϕ is

$$p_\delta(\delta|\phi)\,\mathrm{d}\delta = p_\delta(\delta|\phi)\,\phi\,\mathrm{d}\sin(\theta) = p_\theta(\theta)\,\mathrm{d}\theta = \frac{2\,\mathrm{d}\theta}{\pi}, \tag{A.1}$$

so

$$p_\delta(\delta|\phi) = \frac{2\,\mathrm{d}\theta}{\pi\,\phi\,\mathrm{d}\sin\theta} = \frac{2}{\pi\,\phi\,\cos\theta} = \frac{2}{\pi\,\phi\,(1-\sin^2\theta)^{1/2}} = \frac{2}{\pi(\phi^2-\delta^2)^{1/2}} \quad (\delta \le \phi) \tag{A.2}$$

For an isotropic distribution of jets, the probability distribution of polar angles ϕ is $p_\phi(\phi)\mathrm{d}\phi = \sin\phi\,\mathrm{d}\phi$.

The differential probability distribution of δ for all jets is obtained by integrating over ϕ.

$$p(\delta) = \int_\delta^{\pi/2} p_\delta(\delta|\phi)\,p_\phi(\phi)\,\mathrm{d}\phi. \tag{A.3}$$

Thus, the differential distribution is

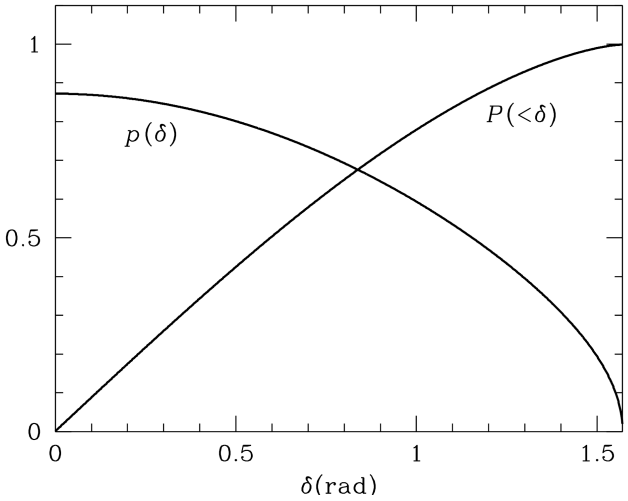

Fig. A.1. Differential probability distribution $p(\delta)$ of the PA difference δ between the disk normal and isotropic radio jets for edge-on maser disks and the cumulative distribution $P(<\delta)$ of PA differences smaller than δ.

$$p(\delta) = \frac{2}{\pi}\int_\delta^{\pi/2} p_\delta\,\frac{\sin\phi\,\mathrm{d}\phi}{(\phi^2-\delta^2)^{1/2}} \tag{A.4}$$

and the corresponding cumulative distribution is

$$P(<\delta) = \int_0^\delta p(\acute{\delta})\,\mathrm{d}\acute{\delta}. \tag{A.5}$$

Both $p(\delta)$ and $P(<\delta)$ are plotted in Fig. A.1.